Research Article

Dosimetric accuracy of delivering SBRT using dynamic arcs on Cyberknife

5

James L Bedford, Simeon Nill and Uwe Oelfke

Joint Department of Physics, The Institute of Cancer Research and The Royal Marsden NHS Foundation Trust, London SM2 5PT, UK.

10

Corresponding author:

James L Bedford,

Joint Department of Physics,

15   The Royal Marsden NHS Foundation Trust,

Downs Road,

Sutton,

Surrey SM2 5PT,

UK.

20   Tel. +44 20 8661 3477

Fax +44 20 8643 3812

Email James.Bedford@icr.ac.uk

ABSTRACT

25 **Purpose:** Several studies have demonstrated potential improvements in treatment time
through the use of dynamic arcs for delivery of stereotactic body radiation therapy (SBRT) on
Cyberknife. However, the delivery system has a finite accuracy, so that potential exists for
dosimetric uncertainties. This study estimates the expected dosimetric accuracy of dynamic
delivery of SBRT, based on realistic estimates of the uncertainties in delivery parameters.

30 **Methods:** Five SBRT patient cases (prostate A - conventional, prostate B - brachytherapy-
type, lung, liver, partial left breast) were retrospectively studied. Treatment plans were
produced for a fixed arc trajectory using fluence optimization, segmentation and direct
aperture optimization. Dose rate uncertainty was modeled as a smoothly varying random
fluctuation of ±1.0%, ±2.0% or ±5.0% over a time period of 10 s, 30 s or 60 s. Multileaf
35 collimator uncertainty was modeled as a lag in position of each leaf up to 0.25 mm or 0.5 mm.
Robot pointing error was modeled as a shift of the target location, with the direction of the
shift chosen as a random angle with respect to the multileaf collimator and with a random
magnitude in the range 0.0 – 1.0 mm at the delivery nodes and with an additional random
magnitude of 0.5 – 1.0 mm in between the delivery nodes. The impact of the errors was
40 investigated using dose-volume histograms.

Results: Uncertainty in dose rate has the effect of varying the total monitor units delivered,
which in turn produces a variation in mean dose to the planning target volume. The random
sampling of dose rate error produces a distribution of mean doses with a standard deviation
proportional to the magnitude of the dose rate uncertainty. A lag in multileaf collimator
45 position of 0.25 mm or 0.5 mm produces a small impact on the delivered dose. In general, an
increase in the PTV mean dose of around 1% is observed. An error in robot pointing of the
order of 1 mm produces a small increase in dose inhomogeneity to the planning target
volume, sometimes accompanied by an increase in mean dose by around 1%.

Conclusions: Based upon the limited data available on the dose rate stability and geometric

50   accuracy of the Cyberknife system, this study estimates that dynamic arc delivery can be

accomplished with sufficient accuracy for clinical application. Dose rate variation produces a

change in dose to the planning target volume according to the perturbation of total monitor

units delivered, while multileaf collimator lag and robot pointing error typically increase the

mean dose to the planning target volume by up to 1%.

55

Keywords: SBRT, SABR, VMAT, arc therapy, delivery accuracy

I. INTRODUCTION

　　　The Cyberknife system (Accuray Inc., Sunnyvale, CA) has shown itself to be a

valuable device for treating patients with stereotactic body radiotherapy (SBRT).[1-4] The

60　　short-waveguide 6-MV flattening-filter-free linear accelerator is mounted on a robotic arm

and is equipped with either a series of circular collimators, a variable circular diaphragm, or a

multileaf collimator (MLC).[5-7] The MLC is widely used to allow treatment of larger tumors

using fewer monitor units.

　　　The Cyberknife currently delivers radiation from a number of static locations around

65　　the patient in a step-and-shoot arrangement.[8] However, a number of studies have

demonstrated the potential for reduction of delivery time by the use of dynamic arc delivery,

similar in nature to volumetric modulated arc therapy (VMAT), although from non-coplanar

orientations as opposed to the more common coplanar arcs used for VMAT. For example,

Kearney et al.[9] describe a non-coplanar arc optimization algorithm for Cyberknife with a

70　　circular collimator. They also describe an optimization method for producing dynamic arcs

on the Cyberknife with MLC, using direct aperture optimization.[10]

　　　Simultaneously, data are beginning to emerge on the accuracy of the Cyberknife

system. Yang et al.[11, 12] describe a calibration procedure for the ArcCheck quality assurance

device (Sun Nuclear, Melbourne, FL) that converts between a spatial error and a dosimetric

75　　error, so that the device can be used to measure the pointing accuracy of the robot. Wang et

al.[13, 14] use a scintillator and charge-coupled device camera to record a pair of spots located on

the beam axis and calculate from these spots the position of the beam to an accuracy in the

order of 0.1 mm. With these data, it is possible to estimate the geometric accuracy of a

dynamic delivery, with a view to determining the dosimetric performance.

80　　　　This study therefore investigates the performance of arc delivery using the Cyberknife

with multileaf collimator, for the case of SBRT. The choice of trajectory is a key aspect of

arc delivery, but as trajectory selection is an extensive subject, the reader is referred to

previous studies for details.[8, 10, 15] In the present study, a previously investigated arc

trajectory[15] is used to provide suitable dynamic baseline plans in the known range of

85   collision-free operation of the Cyberknife robot. Based on published data and other estimates

from Accuray, the expected variations in dose rate, leaf positioning and robot target position

are established and incorporated into models of these parameters (Figure 1). The consequent

impact on the dose distribution is calculated for several cases using these models. Beam

delivery between control points is included in the model so as to give the most accurate

90   possible estimation of the dose distribution.
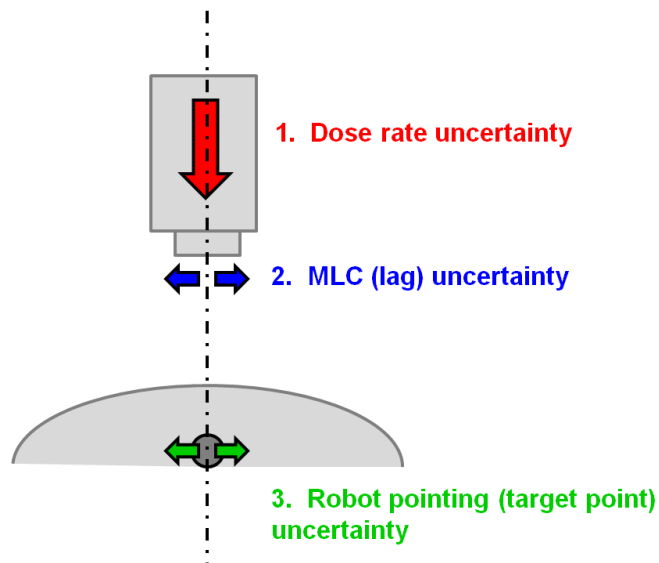
95

Figure 1. Schematic diagram of the uncertainty model used to estimate the dosimetric

accuracy of dynamic arc delivery.

100

II. MATERIALS AND METHODS

II.A. Patient cases

Four patient cases were retrospectively investigated in this study, as follows:

(a) Prostate A, planned for a homogeneous distribution of dose for a prescription of

105   36.25 Gy in 5 fractions according to RTOG 0938.[16] PTV volume 113 cm^3.

(b) Prostate B, the same case planned for a brachytherapy-style dose distribution using

a prescription of 38.0 Gy in 4 fractions.[17, 18] PTV volume 88 cm^3.

(c) Lung, a central lesion prescribed to 50.0 Gy in 5 fractions according to RTOG

0813.[19] PTV volume 14 cm^3.

110   (d) Liver, prescribed to 42.75 Gy in 3 fractions.[20] PTV volume 28 cm^3.

(e) Left partial breast, prescribed to 35.0 Gy in 5 fractions according to RTOG

0413.[21] PTV volume 89 cm^3.

An SBRT technique was used in all cases, with at least 95% of the planning target volume

115   (PTV) being required to receive the prescribed dose. The plans used a fixed isocenter, located

at the center of the PTV.

II.B. Arc trajectory

The arc trajectory used for this study is shown in Figure 2. It was a purpose-made

120   path, distinct from the standard body path used by Cyberknife, and using different node

positions. It consisted of 104 nodes, or control points, with a spacing of 5° in robot

orientation. The trajectory was designed by an Accuray heuristic to give a uniform coverage

of the space around the patient, while respecting hardware constraints on collisions and

cabling. The performance of the arc in comparison with the standard body path was
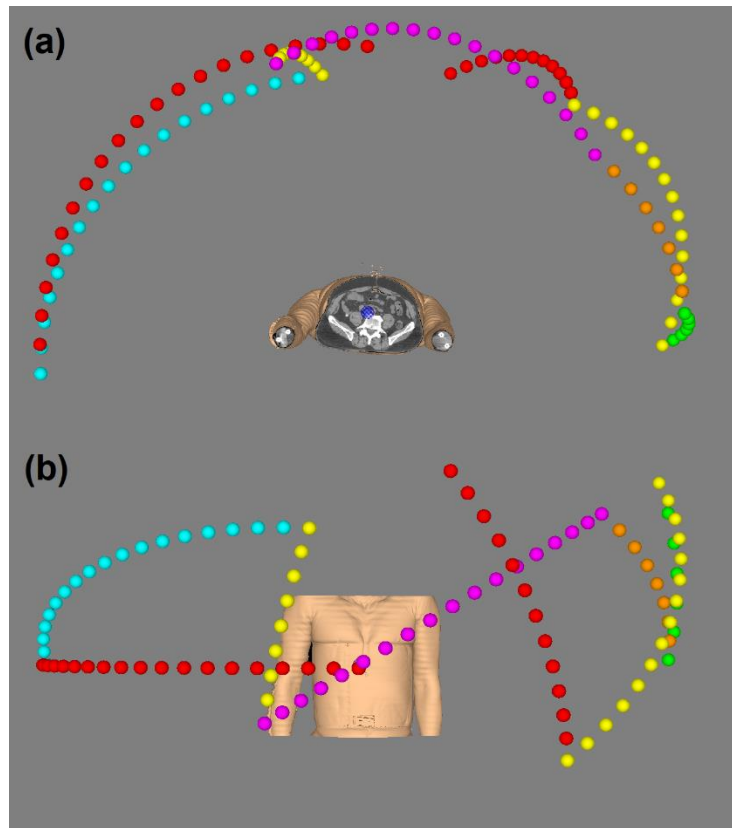
125   previously investigated.[15]

Figure 2. The trajectory used for the dynamic arc plans, illustrated for the liver case. The points give the positions of the radiation source. (a) view from inferior, (b) view from anterior.

130

II.C. Dose calculation and optimization scheme

Dose was calculated as:

$$d_i = \sum_j d_{ij} w_j \tag{1}$$

135

where d_i was the dose at voxel i in the patient model, d_{ij} was the dose contributed by beamlet j to voxel i, and w_j was the beamlet weight. The dose calculation was based on an Accuray-supplied pencil-beam algorithm embedded into an in-house computation and optimization framework. The commercial planning system for Cyberknife was not used in this study. The

140 dose-influence matrices, d_{ij}, of equation (1) were calculated by using this algorithm to

calculate the dose for a series of bixel-sized fields. The dose grid was $2 \times$ CT pixel size in the

transaxial direction and CT slice spacing in the longitudinal direction. Dose voxels which

received less than 0.015% of the maximum dose of each d_{ij} component were neglected so as

to minimize the size of the dose matrices.

145   Plans were produced for all of the cases using a three-step optimization scheme which

produced fluence maps, then sequenced these into deliverable apertures, before performing

direct aperture optimization. The resolution of the fluence map was 7.7 mm $\times$ 5.0 mm at a

nominal source-axis distance of 800 mm, the 7.7 mm being equal to two leaf widths so that

the MLC leaves could be paired.[8] This was a practical feature designed to reduce the number

150 of fluence bixels and hence reduce memory requirements and increase optimization speed.

The optimization minimized an objective function, F, defined as:

$$F = \sum_k f_k ,$$

(2)

155 where the indices, k, referred to individual anatomical structures, each with objective value f_k:

$$f_k = a_k \left[d_i^{\min} - d_i \right]_{\geq 0}^2 + b_k \left[d_i - d_i^{\max} \right]_{\geq 0}^2 .$$

(3)

In this equation, the variables a_k and b_k referred to the importance factors for structure k.

160 Fluence was optimized using the L-BFGS optimization scheme, which was a standard

gradient descent method using a recursion relation for calculation of search directions, so as

to avoid having to store a large and memory-intensive inverse Hessian matrix.[22]

A fluence map was produced by the optimizer for every third beam orientation. After fluence optimization using 40 iterations, the plan was sequenced using a well-established sequencer,[23] with three apertures being used to account for each fluence map. Two of these apertures were redistributed to the beam orientations either side of that for which fluence was optimized. The L-BFGS method was again used for the direct aperture optimization, with each aperture shape being used to define which fluence pixels were active, and then with the corresponding bixel doses being used to calculate dose and search directions.[22,24] The optimization itself was therefore based on dose calculated by summation of bixel doses.

During the direct aperture optimization, the method of Christiansen et al.[25] was used to model the motion of MLC leaves between control points. The motion of one leaf in a leaf pair produced a fluence ramp in one direction, and the motion of the opposing leaf produced a ramp of fluence in the other direction, and the total fluence was calculated as the difference between the two fluence patterns.

The direct aperture optimization also took into account the delivery constraints of the Cyberknife.[15] The approach taken was that the robot speed was given first priority, defining the delivery time for the arc. The robot speed was taken as 60 mms^{-1}, equivalent to the slowest speed observed in practice, so that the time to traverse 5° of arc was calculated to be 1.5 s. The MLC movement was then limited so that the time for MLC motion should not exceed the time taken by the robot to make its movement. The MLC leaf speed was taken to be 33 mms^{-1}, which was slightly faster than in current clinical practice, but a speed which was advised by Accuray to be achievable using the current generation of hardware. In the 1.5 s taken for the robot to traverse between nodes, the MLC leaves were therefore able to move 50 mm, and this limit was used by the optimizer. There was no limit to the minimum monitor units per segment, implying that the beam could be paused if required. There was also no limit on the maximum monitor units per segment, which meant that if the time for delivery of

the monitor units was large, it could exceed the time taken for the robot motion. In practice,

the robot would slow down in this situation. Further details of the optimization scheme are

190   given elsewhere.[15]

After the optimization, dose was recalculated using the Accuray dose calculation in

the local computational framework, based on complete apertures rather than on the sums of

bixel doses used during the optimization. The dose grid resolution used for this recalculation

was the same as for the bixel-based dose calculation used during optimization. The

195   recalculated aperture dose had a very similar relative dose distribution to the original bixel-

based dose produced by the optimizer, but was seen to be offset by a case-specific factor of

several percent. This resulted from the difference between calculating dose due to MLC-

shaped apertures and due to collections of individual 7.7 mm $\times$ 5 mm apertures. The aperture

dose was actually the more accurate dose, but as the treatment plans had been created and

200   clinical constraints had been met using bixel-based doses, the recalculated plan was

renormalized to return the dose approximately to the bixel-based dose distribution, so that the

clinical constraints were met as closely as possible. Since the difference between the

aperture-based and bixel-based doses was a relative scaling, this renormalization was

accomplished by multiplying the aperture dose by a simple scale factor. The same

205   renormalization factor was used for all plans in each patient case, so that this did not

confound any changes in dose resulting from the errors examined in the study. Throughout

the study, the monitor units calculated by the optimization engine were used, without any

application of a scale factor.

In the final dose recalculation, additional nodes were used to model the robot

210   orientation and MLC leaf position as accurately as possible. Four intermediate nodes were

added between each pair of nodes, such that the additional nodes, together with the second of

the original pair of nodes, formed a set of five interpolated nodes.[15] A further 20 equally-

weighted interpolated apertures, allowing for MLC leaf motion, were calculated between each

of the interpolated nodes, and dose was then calculated and summed for all of the interpolated

215   apertures (Figure 3). This detailed modeling of the MLC motion was found previously to be

essential for accurate dose calculation with relatively large movements of small apertures.[26]
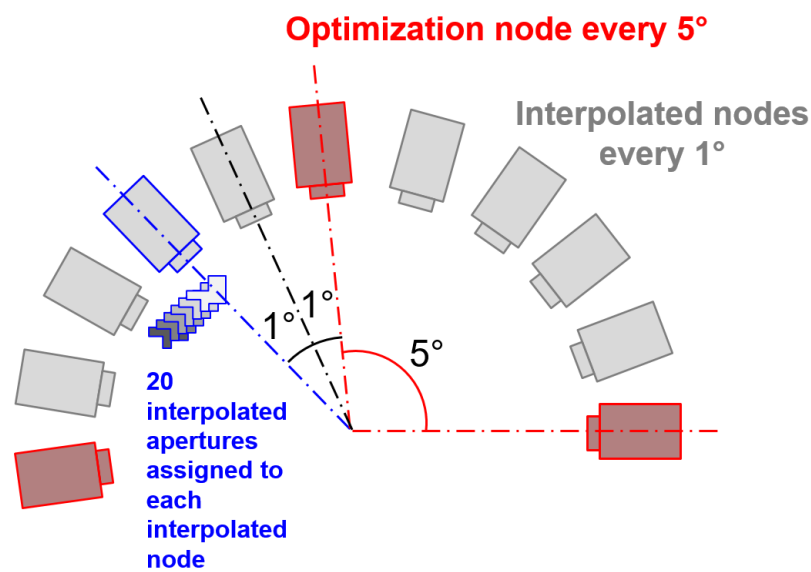
220

Figure 3. The model for control point interpolation. There are four interpolated nodes

between each optimization node. The 20 interpolated apertures between each interpolated

node allow for the modeling of MLC leaf motion and are all assigned to the following

interpolated node.

225

230

II.D. Uncertainty models

The uncertainty models are described below. The uncertainties were considered independently so as to determine their individual contributions to the delivery uncertainty.

235   ### II.D.1. *Dose rate uncertainty*

Dose rate variations were modeled as a series of pseudorandom errors defined at integer numbers of the error period, which was set to 10 s, 30 s or 60 s in turn (Figure 4). The first of these values represented a rapidly drifting error and the last represented a slowly drifting error. The errors were sampled from a uniform distribution spanning from $-E$ to $+E$, where E was the error magnitude, which was either 0.01 (i.e. 1%), 0.025 or 0.05. Between the error sampling points, the error was determined by linear interpolation. Large and abrupt changes (e.g. due to arcing) were ignored.
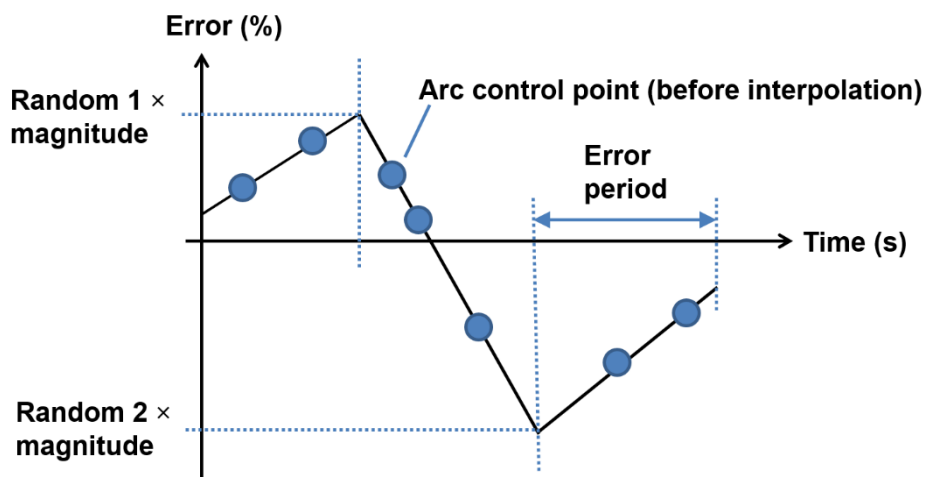
245

Figure 4. The dose rate uncertainty model.

Addition of the random errors to the treatment arcs was carried out using the 104-node

250   optimized plans, before addition of interpolated nodes. The time, t_n, at which segment n ($n =$

1…104) of the arc took place was calculated according to the formula:

$$t_n = \sum_{i=1}^{n} \max\left(\frac{60}{D} M_i, T_R\right),$$ (4)

255   where M_i was the number of monitor units per fraction at node i, $D = 1000$ monitor units per

minute was the maximum dose rate of the linear accelerator, and $T_R = 1.5$ s was the robot

traversal time. In other words, the time taken to deliver each segment of the arc was equal to

the fixed traversal time T_R, unless the monitor units, delivered at maximum dose rate, required

additional time for delivery, in which case the time was equal to the time to deliver the

260   monitor units. According to the time that a given control point was delivered, the appropriate

value of error was determined from the error model. The monitor units for that control point

were changed by the error:

$$M_E = M_i + E \cdot M_i,$$ (5)

265

where M_i were the monitor units before addition of the error, M_E were the monitor units after

addition of the error, and E was the error. Strictly speaking, the delivery of M_E monitor units

took a different length of time to delivering M_i monitor units, thereby influencing the time at

which the error, E, should be sampled, but this secondary effect was neglected. Using M_E,

270   five interpolated nodes, each with 20 interpolated apertures, were calculated as described

above. The three error periods and three error magnitudes gave nine combinations of error.

For each combination of error period and magnitude, the calculation was repeated 10 times to give an indication of the spread of outcomes resulting from the selection of random errors.

275

II.D.2. MLC position uncertainty

To model MLC leaf position uncertainty, at each control point of the arc (before interpolation), the position of each MLC leaf was moved 0.25 mm towards its position at the previous control point. The MLC leaf positions and the movement of 0.25 mm were defined

280   at the nominal source-axis distance of 800 mm. If the position of the MLC leaf at the previous control point was less than 0.25 mm away from its position at the current control point, the leaf was only moved as far as the position at the previous control point. This limitation occurred for between 4% and 13% of leaf movements, depending on the patient case, when considering all MLC leaves at all control points and neglecting closed leaf pairs.

285   No change in position occurred for the first control point in the arc. The direction of MLC perturbation (i.e. use of a lag in position) and the representative magnitudes of uncertainty were based on worst-case observations of the physical Cyberknife device.

After the change in position had been effected, five interpolated nodes, each with 20 intermediate apertures, were introduced and the dose was calculated, based on the interpolated

290   plan. The experiment was repeated with a lag of 0.5 mm.

II.D.3. Robot pointing uncertainty

Each robot position was specified by a source point and target point, the target point corresponding to the isocenter on a conventional linear accelerator, but in this case varying in

295   source-target distance. To model the uncertainty in robot pointing, at each control point of the arc (before interpolation), the target point of the node was moved according to a uniformly sampled random direction with respect to the multileaf collimator. The error directions of the

interpolated control points were then computed by linear interpolation between these

directions. The interpolated directions were chosen to take the shortest route around the error

300   circle (Figure 5).

        The magnitude of the error at the nodes before interpolation was uniformly sampled

from $0 \ldots N$, where N was either 0 mm or 1 mm. It was expected that the positioning of the

robot would be less accurate between nodes than at the actual node positions, since between

nodes, the control system would be carrying out some form of interpolation. An additional

305   uniformly sampled error of $0 \ldots M$ was therefore added midway between the nodes, to reflect

the additional uncertainty between nodes, where M was either 0.5 mm or 1.0 m. The total

error was thus $(n_1 + n_2)/2 + m$ at the mid-point between the nodes, where n_1 and n_2 were

randomly sampled from a uniform distribution of width N and m was randomly sampled from

a uniform distribution of width M. The magnitude of the error between the original nodes and

310   the midpoint between them was calculated by linear interpolation, so that the total error

changed smoothly from n_1 to $(n_1 + n_2)/2 + m$ and then smoothly to n_2.

II.D.4. *Combination of uncertainties*

        The above uncertainties were applied individually to the treatment plans, but their

315   impact if they were all present simultaneously was also investigated. A dose rate uncertainty

of magnitude 0.025 with a time period of 30 s, an MLC lag of 0.25 mm and a robot pointing

uncertainty of 1.0 mm at nodes with an additional uncertainty of 0.5 mm between nodes was

used for this investigation. All of the uncertainties were applied to the same treatment plan

and the effect on the dose distribution was observed. Three runs were carried out to assess the

320   impact of the random variations.

A summary of the numerical values of uncertainty used in the model, together with their sources, is given in Table I.
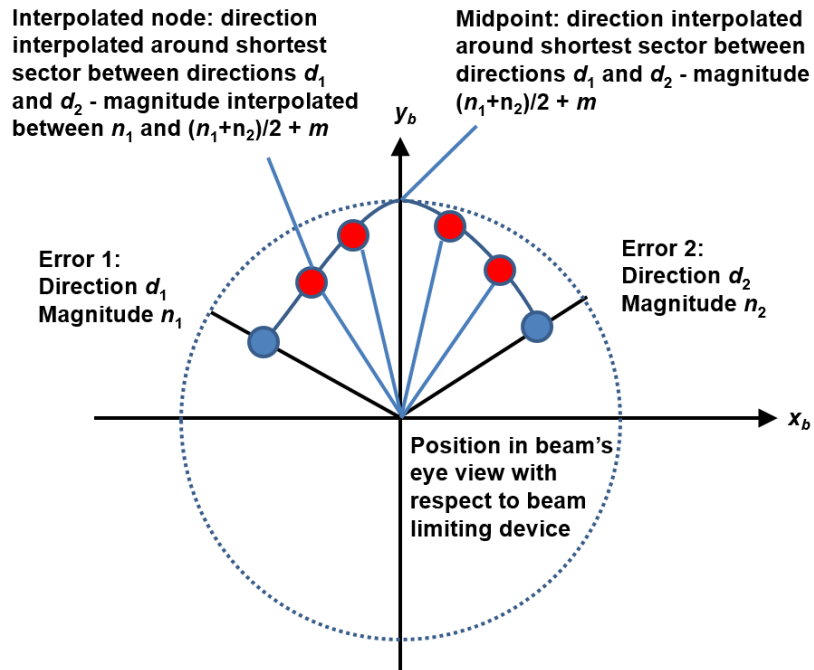
325

Figure 5. Model for robot pointing uncertainty. The axes are labelled according to IEC 61217 convention and the directions are defined relative to the $-y_b$ axis.

330

335

Table I. Values and sources of uncertainty used in this work.

Uncertainty	Numerical values	Sources
Dose rate uncertainty	1%, 2.5% or 5% random variations over a time period of 10 s, 30 s or 60 s	Accuray suggested
MLC lag uncertainty	0.25 mm or 0.5 mm lag in MLC position at nominal source-axis distance of 800 mm	Accuray internal observations
Robot pointing uncertainty	- Direction with respect to MLC: random between 0° and 360° - Magnitude at nodes: 0.0 mm or random between 0.0 mm and 1.0 mm - Additional magnitude between nodes: random between 0.0 mm and 0.5 mm or between 0.0 mm and 1.0 mm	Yang et al.[11, 12] Wang et al.[13] Wang and Nelson[14]
Combination	- 2.5% random variation of dose rate over a time period of 30 s - 0.25 mm lag in MLC position at nominal source-axis distance of 800 mm - Robot pointing uncertainty random between 0.0 mm and 1.0 mm at nodes and additionally random 0.0 mm to 0.5 mm between nodes	All of the above

340

III. RESULTS

III.A. Optimized treatment plans

The calculated monitor units and estimated delivery times for the five arcing treatment

plans are given in Table II. The estimated delivery times are calculated using equation (4) for

the final node, and the corresponding times for static delivery are also shown. Representative

dose distributions for the treatment plans without delivery uncertainties are shown in a

previous study, together with more details of comparison with static delivery.[15]

III.B. Dose rate uncertainty

The variation in monitor units per fraction with control point for the prostate A case, and the

random uncertainty from the uncertainty model, are shown in Figure 6. The error distribution

Table II. Total monitor units per fraction and estimated delivery time per fraction for the five

patient plans in the absence of uncertainty. For comparison purposes, the estimated static

delivery time is also included.

	MU PER FRACTION	ESTIMATED DELIVERY TIME (s)	ESTIMATED STATIC DELIVERY TIME (s)
Prostate A	4978	355	675
Prostate B	10579	672	1025
Lung	4312	290	672
Liver	9368	584	965
Partial breast	2833	235	554

360   (Figure 6b) varies from run to run, due to the selection of a different set of random numbers

each time. The results of 10 runs of the calculation are shown in Figure 7 for 5% uncertainty

at time periods of 10 s, 30 s and 60 s. The graphs show a range of doses to the PTV, and this

also occurs for the other patients. The statistics for the runs giving the lowest and highest

doses are shown for all patients in Table III with 5% uncertainty and a time period of 60 s, i.e.

365   for the situation in Figure 7c.

The variation in PTV dose is accompanied by a variation in total monitor units per

fraction. The predominant effect of the random variation of the monitor units is to change the

total number of monitor units delivered, and this correlates closely with the variation in dose

to the PTV (Figure 8). The longer time period results in fewer random samples of error over

370   the length of the delivery, so that the errors are less likely to cancel than with many samples.

Consequently, the longer time period gives rise to a larger fluctuation in PTV dose than with

the shorter time period.

(a)

(b)
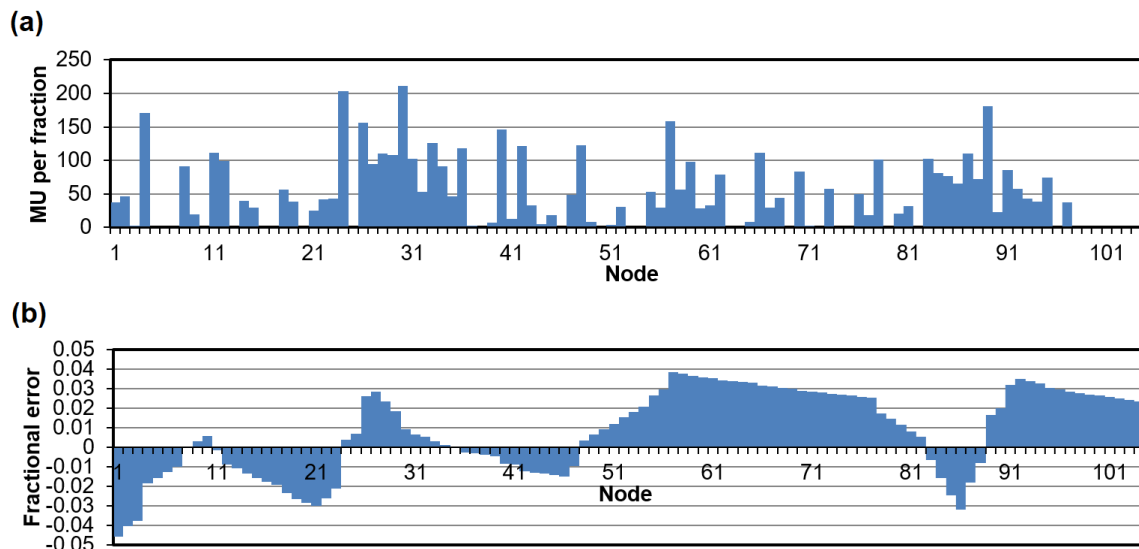
375   **Figure 6.** (a) Monitor units per fraction for prostate A as a function of delivery node. (b) The

fractional error applied to the monitor units, using an error magnitude of 5% and a time period
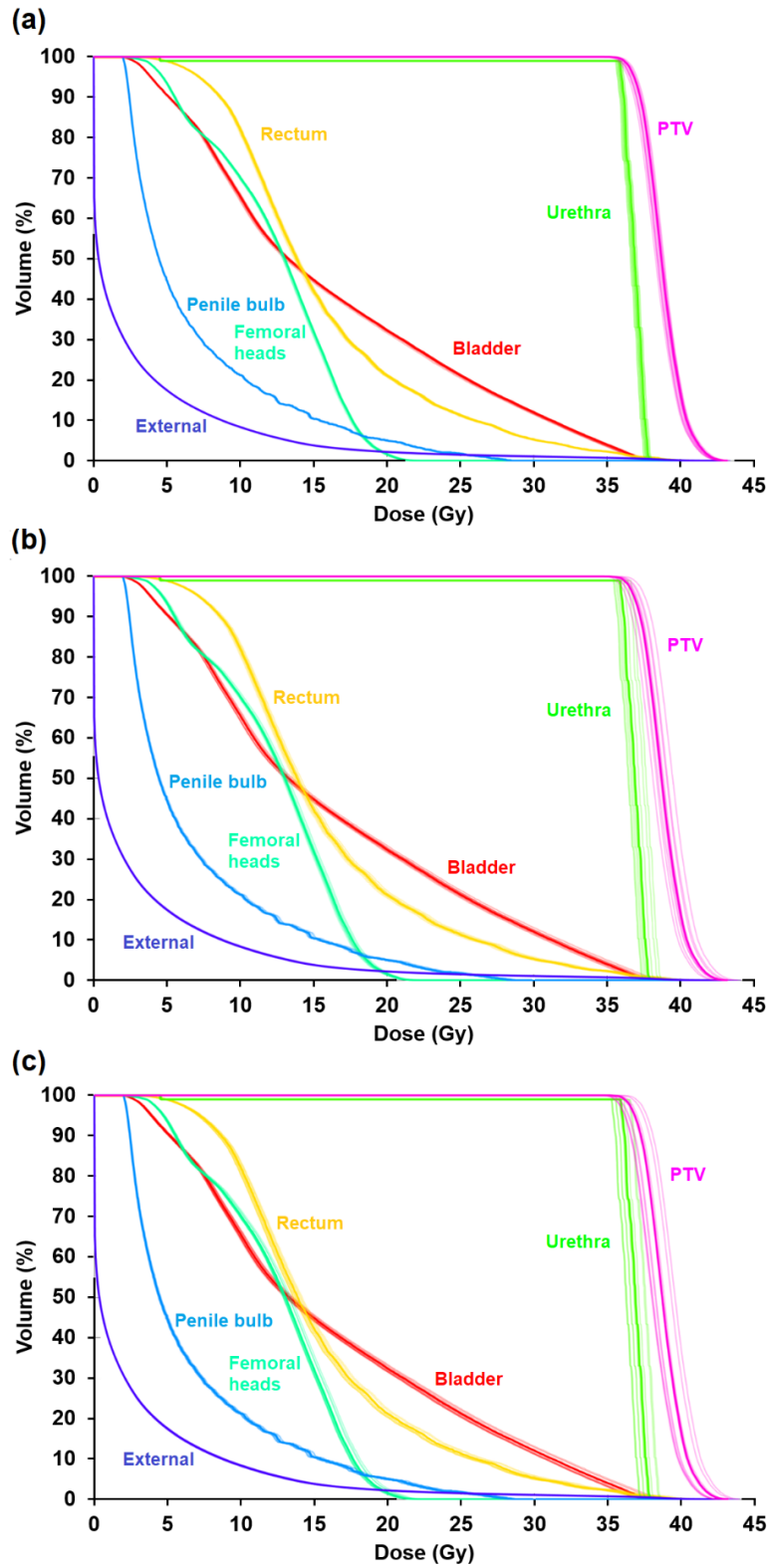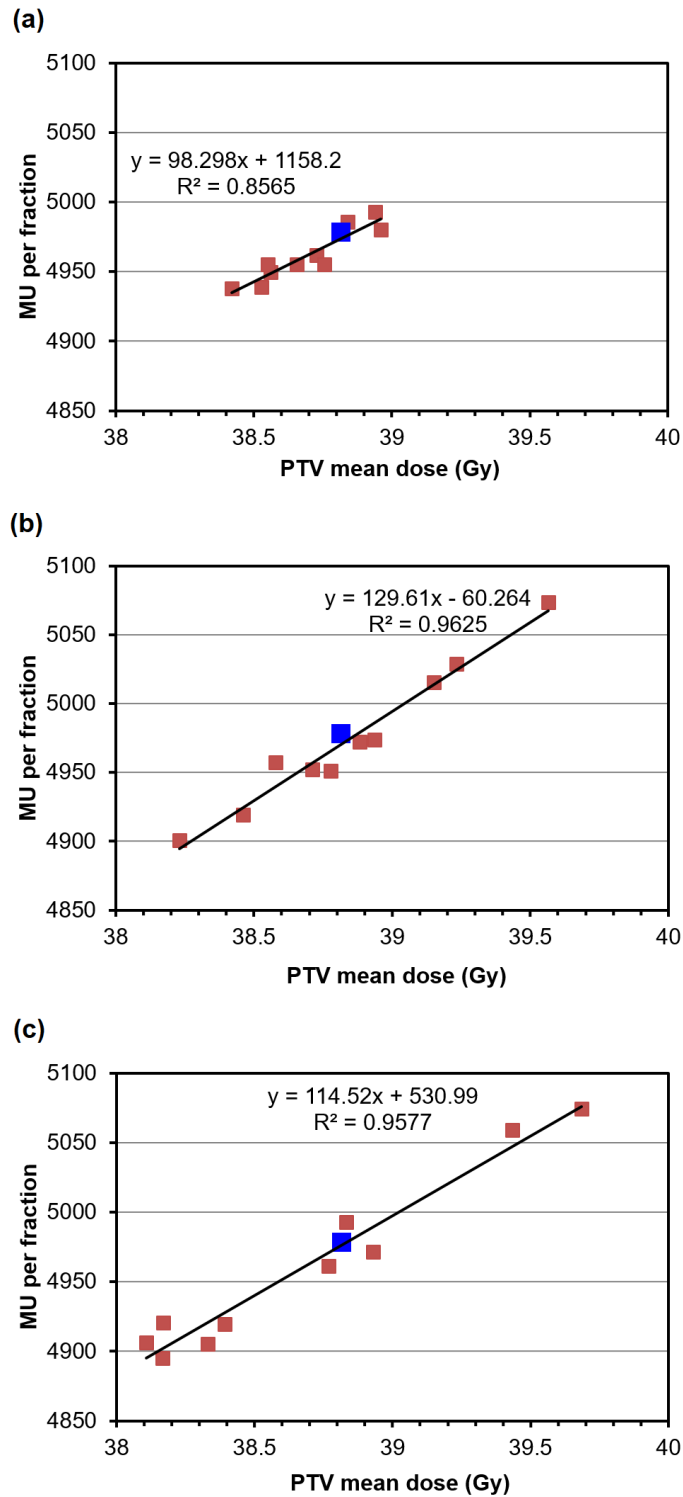
of 30 s.

Figure 7. Dose-volume histograms for prostate A for 10 calculations, with error uncertainty of 5% using a time period of (a) 10 s, (b) 30 s and (c) 60 s. The bold lines represent the dose-volume histograms without uncertainty.

Table III. PTV statistics for the runs giving the lowest and highest PTV doses with 5% dose rate uncertainty and a time period of 60 s (see Figure 7c).

CASE	RUN	PTV mean dose (Gy)	PTV min dose (Gy)	PTV max dose (Gy)
Prostate A	No error	38.81	35.35	43.26
	Minimum	38.11	34.70	42.53
	Maximum	39.69	36.19	44.08
Prostate B	No error	54.42	29.50	93.65
	Minimum	53.36	28.98	92.00
	Maximum	55.39	30.03	95.32
Lung	No error	55.83	45.46	62.42
	Minimum	54.52	44.36	60.99
	Maximum	56.72	46.16	63.43
Liver	No error	51.01	40.05	59.90
	Minimum	49.91	39.26	58.66
	Maximum	52.12	40.77	61.39
Partial breast	No error	39.01	32.48	45.23
	Minimum	37.93	31.66	43.91
	Maximum	39.55	33.04	45.82

385

(a)

(b)

(c)

390 **Figure 8.** Correlation between PTV mean dose and total monitor units per fraction for prostate A for 10 calculations, with error uncertainty of 5% using a time period of (a) 10 s, (b) 30 s and (c) 60 s. The blue square represents the plan without uncertainty and the line shows a linear fit to the data.

The other error magnitudes of 0.01 and 0.025 give similar results to an error

395   magnitude of 0.05, but with a correspondingly scaled down effect. The standard deviation of

the error is expected to be proportional to the error magnitude, so a curve of the form

$\sigma = M \sqrt{aT^2 + bT}$ is fitted to the graphs of standard deviation versus error magnitude, where

σ is the standard deviation, in Gy, of the PTV mean dose, M is the magnitude of the dose rate

error, as a dimensionless proportion of the correct dose rate, and T is the time period, in

400   seconds, of the dose rate variation. The values of a and b are constant and to be determined.

By first plotting σ against M for several values of T and then fitting a polynomial of the form

$aT^2 + bT$ to a plot of the squared gradient of these curves against T, the behavior is found to

be modeled by the equation:

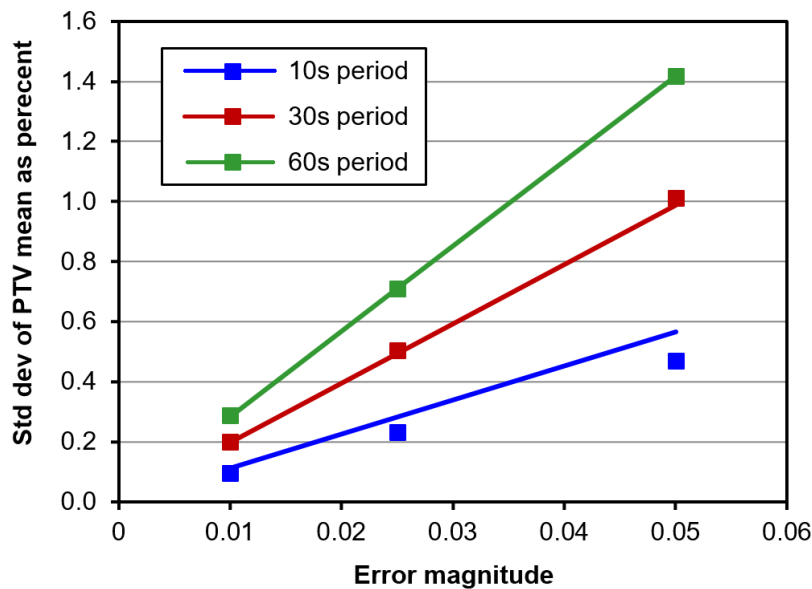405 $$\sigma = M \sqrt{0.0018T^2 + 1.9084T} \ . \qquad\qquad (6)$$

As a percentage of the PTV mean dose for the plan without errors, the relationship between

standard deviation and error magnitude and period is:

410    $$\sigma = M \sqrt{0.0121T^2 + 12.666T} \ , \qquad\qquad (7)$$

where σ is now the standard deviation of the PTV mean dose, as a percentage of the correct

PTV mean dose. The overall variation of PTV mean dose is shown in Figure 9 for the

prostate A case, with the modeled results using this equation included. The results of

415   applying equation (7) to all of the patient cases are shown in Table IV for the largest error

magnitude.

For context, the observed data are based on a sample size of 10, so the standard error

of the actual standard deviation, σ, shown in Figure 9 and Table IV is $\sigma/\sqrt{2(n-1)} \approx \sigma/4$. In

other words, the inherent variability of the data is approximately one quarter of the standard

420   deviations given.

425

Figure 9. Standard deviation of PTV mean dose as a function of the magnitude and period of

dose rate error for the prostate A case. The standard deviation of PTV mean dose is expressed

as a percentage of the PTV mean dose for the plan without errors. The squares show the

430   observed standard deviation of PTV mean dose, and the lines show the result of using

equation (7).

Table IV. Standard deviation of PTV mean dose as a function of dose rate error magnitude

435 and error period. For all cases except the first, only the results for worst case error

magnitudes and periods are shown. For each combination of magnitude and period the actual

variation of PTV mean dose observed in 10 random plans is compared against the variation

predicted by equation (7).

| CASE	MAGNITUDE	PERIOD (s)	PREDICTED % SD	ACTUAL % SD
Prostate A	0.01	10	0.11	0.10
	0.01	30	0.20	0.20
	0.01	60	0.28	0.29
	0.025	10	0.28	0.23
	0.025	30	0.49	0.50
	0.025	60	0.71	0.71
	0.05	10	0.57	0.47
	0.05	30	0.99	1.01
	0.05	60	1.42	1.42
Prostate B	0.05	60	1.42	1.10
Lung	0.05	60	1.42	1.37
Liver	0.05	60	1.42	1.29
Partial breast	0.05	60	1.42	1.26

440

III.C. MLC position uncertainty

Dose-volume histograms showing the impact of a 0.5 mm MLC lag are shown in

445 Figure 10 for the prostate B and lung cases. (Due to the large overlap of the PTV with the

proximal bronchus in the lung case, the plan is unable to meet the constraint that the dose to 4

cm^3 of proximal bronchus should not exceed 18 Gy.) The MLC lag has the effect of

modifying the dose to the PTV by around 1%, with a slightly larger effect on the urethra in

the prostate B case. Table V shows the statistics for all of the cases, for both 0.25 mm and 0.5

450   mm lag.
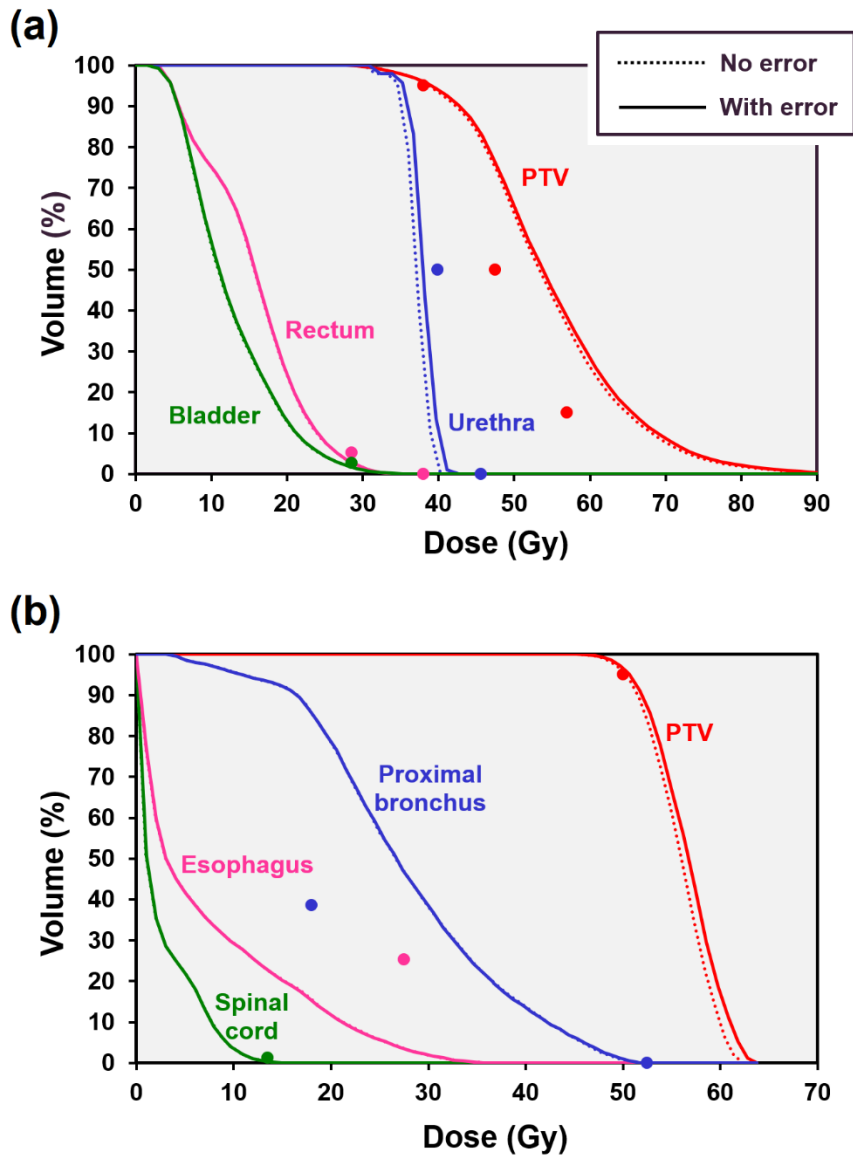
455   **Figure 10.** Dose-volume histograms showing the impact of a 0.5 mm MLC lag on the

treatment plans for (a) prostate B case, and (b) central lung case. Solid lines: with MLC lag,

dotted lines: without MLC lag. The points represent the principal clinical constraints.

Table V. PTV statistics as a function of MLC lag.

CASE	RUN	PTV mean dose (Gy)	PTV min dose (Gy)	PTV max dose (Gy)
Prostate A	No error	38.81	35.35	43.26
	0.25 mm lag	38.97	35.37	43.55
	0.5 mm lag	39.12	35.35	43.91
Prostate B	No error	54.42	29.50	93.65
	0.25 mm lag	54.73	29.51	94.88
	0.5 mm lag	54.97	29.44	95.59
Lung	No error	55.83	45.46	62.42
	0.25 mm lag	56.22	45.45	63.15
	0.5 mm lag	56.58	45.38	63.79
Liver	No error	51.01	40.05	59.90
	0.25 mm lag	51.18	39.92	60.36
	0.5 mm lag	51.35	39.83	60.82
Partial breast	No error	39.01	32.48	45.23
	0.25 mm lag	39.20	32.47	45.67
	0.5 mm lag	39.39	32.43	46.07

460

III.D. Robot pointing uncertainty

The effect of a randomly sampled robot pointing error of 1.0 mm at the delivery

465 nodes, with an additional randomly sampled error 1.0 mm between the nodes is shown in

Figure 11 for the liver and partial breast cases. The effect of the error is to modify the PTV

dose slightly, with an increase in dose usually being observed. Table VI shows the statistics

for all cases and robot pointing errors.
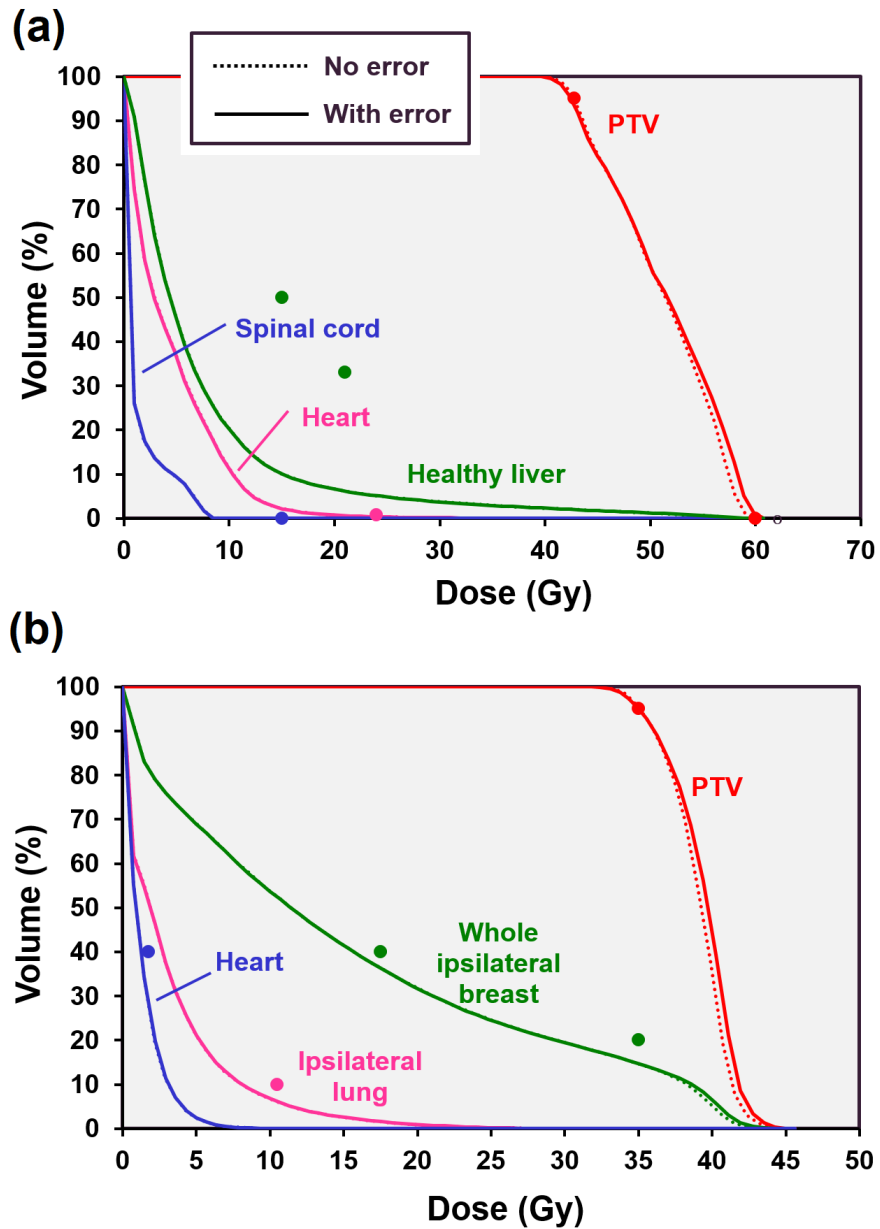
470

Figure 11. Dose-volume histograms showing the impact of a robot pointing error of 1.0 mm

at nodes and an additional error of 1.0 mm between nodes, for (a) liver case, and (b) partial

breast case. Solid lines: with pointing error, dotted lines: without pointing error. The points

475   represent the principal clinical constraints.

Table VI. PTV statistics as a function of robot pointing error.

480

CASE	NODE ERROR (mm)	ADDITIONAL INTER-NODE ERROR (mm)	PTV mean dose (Gy)	PTV min dose (Gy)	PTV max dose (Gy)
Prostate A	0.0	0.0	38.81	35.35	43.26
	0.0	0.5	39.14	35.35	44.02
	0.0	1.0	39.13	35.37	43.94
	1.0	0.5	39.12	35.35	43.97
	1.0	1.0	38.94	35.19	43.88
Prostate B	0.0	0.0	54.42	29.50	93.65
	0.0	0.5	54.97	29.53	95.58
	0.0	1.0	54.94	29.58	95.74
	1.0	0.5	54.95	29.21	95.45
	1.0	1.0	54.89	29.35	96.22
Lung	0.0	0.0	55.83	45.46	62.42
	0.0	0.5	56.61	45.44	63.77
	0.0	1.0	56.62	45.35	63.85
	1.0	0.5	56.54	45.54	63.51
	1.0	1.0	56.64	45.35	64.08
Liver	0.0	0.0	51.01	40.05	59.90
	0.0	0.5	51.35	39.86	60.80
	0.0	1.0	51.32	39.67	60.80
	1.0	0.5	51.30	39.82	61.02
	1.0	1.0	51.27	39.30	60.78
Partial breast	0.0	0.0	39.01	32.48	45.23
	0.0	0.5	39.37	32.50	46.04
	0.0	1.0	39.38	32.48	46.06
	1.0	0.5	39.34	32.22	46.23
	1.0	1.0	39.36	32.34	45.67

III.E. Combination of uncertainties

The effect of a dose rate uncertainty of magnitude 0.025, an MLC lag of 0.25 mm and
485   a robot pointing uncertainty of 1.0 mm with an additional 0.5 mm between nodes, is to adjust

the PTV mean dose by around 1%, mostly with the minimum and maximum doses following

the trend of the mean dose. The results of three runs for each patient are shown in Table VII.

Table VII. PTV statistics for three runs with a combination of dose rate, MLC lag and robot
490   pointing errors.

CASE	RUN	PTV mean dose (Gy)	PTV min dose (Gy)	PTV max dose (Gy)
Prostate A	No error	38.81	35.35	43.26
	Run 1	38.71	35.15	43.23
	Run 2	39.08	35.47	43.80
	Run 3	38.89	35.41	43.44
Prostate B	No error	54.42	29.50	93.65
	Run 1	54.48	29.68	94.23
	Run 2	54.76	29.43	94.62
	Run 3	54.51	29.66	94.45
Lung	No error	55.83	45.46	62.42
	Run 1	55.49	45.13	62.31
	Run 2	56.21	45.52	62.99
	Run 3	56.15	45.58	63.30
Liver	No error	51.01	40.05	59.90
	Run 1	50.84	39.83	60.02
	Run 2	51.33	39.90	60.92
	Run 3	51.05	39.73	60.03
Partial breast	No error	39.01	32.48	45.23
	Run 1	38.89	32.30	44.98
	Run 2	39.21	32.19	45.86
	Run 3	39.08	32.30	45.62

IV. DISCUSSION

The ability of the Cyberknife system to treat from a variety of non-coplanar beam directions[27] is useful for high-quality treatment of SBRT.[1-4] Treating from such a range of orientations is time-consuming, so that the total treatment time is long. However, several recent studies have shown that use of a dynamic arc delivery can reduce the treatment time by a factor of approximately two. For example, Kearney et al.[10] report for prostate and brain patients a speedup of 1.5 ± 0.3, depending on the parameters used by the optimizer, and Bedford et al.[15] report a median speedup of 1.90 (range 1.53 to 2.36). Similarly, using a C-arm linear accelerator, Wild et al.[24] predict a delivery time of 6.5 minutes on average for non-coplanar VMAT. The choice of arc trajectory is likely to have an impact on the delivery time.[28]

Since the Cyberknife does not currently deliver radiation in dynamic mode, it is not possible to measure the dosimetric accuracy of dynamic delivery in the same way that is possible for a C-arm linear accelerator.[28] However, several recent studies have reported on the geometric accuracy of the device, which have been used in the present study to give estimates of the expected dosimetric performance.[11-14] Variations in dose rate are shown to have negligible effect on the shape of the dose distribution, but rather to impact on the total monitor units delivered, which in turn affect the scaling of the plan, most noticeably in the mean dose to the PTV. There is a corresponding effect on the organs at risk in proportion to the dose received by these organs at risk. For example, proximal structures such as the urethra and the proximal bronchus are impacted similarly to the PTV, whereas distal structures are hardly affected at all. The magnitude of the dosimetric error determined in this study is likely to be a worst-case estimate, as the variation in the monitor units produced by the optimizer is quite high (Figure 6), with some nodes not delivering any dose at all.

The impact of an MLC lag is shown to cause a small change in PTV dose. This is almost always in the form of an increase in PTV dose of around 1% for a 0.5 mm lag in MLC leaf position. This is in accord with the work of Christiansen et al.,[25] who demonstrate large changes in PTV dose depending upon whether MLC leaves are considered static at their

520   positions while passing the delivery control points, or dynamic with motion between control points. The present work uses a dynamic beam model throughout, in order to model the dose delivery as accurately as possible, but the comparison of Christiansen et al.[25] with a static situation is very similar to a situation with a severe MLC lag.

In terms of practical measurements on the current generation of Cyberknife, perhaps

525   the most that is known is for the accuracy of robot pointing at static nodes.[11, 12] The effect of a random error in the order of 1.0 mm at control points, with an additional error between control points, is to modify the PTV dose by approximately 1%. An uncertainty in robot position is similar in nature to an uncertainty in MLC leaf position, so the similarities between the results for MLC lag and robot position are rational. The uncertainty in robot pointing is

530   modeled in this study as a shift in the target point, with the robot itself positioned correctly (but not orientated correctly). The results might be affected by using a model in which the robot itself is positioned incorrectly. However, Wang and Nelson[14] show that the overall result of translation and rotation errors is a shift in the target point of less than 1 mm, so the model used in the present study is representative.

535   Taking these results together, the study shows that the Cyberknife is expected to be able to deliver dynamic arc beams with a dosimetric accuracy of the order of 1-2%. This is comparable to accuracy studies for Cyberknife with static beam delivery, on the one hand, and conventional linear accelerators delivering VMAT, on the other hand. For Cyberknife with static beam delivery, Dieterich et al.[29] and Moore et al.[30] recommend a dosimetric

540   accuracy of 90% within 2% and 2 mm in comparison with the treatment planning system.

Some of this tolerance is used by the treatment planning system, but the accuracy predicted by

the present study is within this order of magnitude. Similarly, for coplanar VMAT

delivery,[31-33] Ling et al.[34] report MLC leaf positions generally within 0.5 mm of their

expected position, and relative dose accuracy of 0.7%. Bedford and Warrington[35] report a

545   dynamically delivered dose generally within 2% of the same plan delivered statically, and a

gamma agreement of 3% and 3 mm for delivery of a complete treatment plan. Mans et al.[36]

recommend a dose rate dependence with gantry angle of better than 0.5% and MLC leaf

positioning of better than 1.0 mm and preferably better than 0.5 mm. For comparison with a

treatment planning system, 90% of the delivered dose should be within 3% and 3 mm.

550   The results have been obtained for PTV volumes between 14 cm^3 (lung case) and 113

cm^3 (prostate A case). A larger relative impact is observed with MLC position uncertainty for

the lung case than the prostate A case, which may be partly due to the difference in volume.

It is very likely that different results may occur for very small stereotactic volumes below 10

cm^3, in which case the present results should be treated with caution.

555   The choice of arc trajectory may have some impact on the dosimetric accuracy. The

trajectory used in this study is the result of a heuristic which aims to provide a uniform

coverage of the beam orientation space, while taking into account cabling requirements and

collision avoidance. This trajectory is asymmetric, and has been shown in a previous study[15]

to compare well with the standard (symmetric) body path for the Cyberknife in terms of dose

560   distribution and conformity. The trajectory affects the number of monitor units, the MLC

shapes and the robot positions, and is therefore likely to affect the delivery uncertainties and

hence the dosimetric results of the study to some degree. However, it is thought that the

principal conclusions of this study are likely to be similar whichever trajectory is chosen.

        Further improvement in the delivery accuracy could be obtained by the use of robust

565   treatment planning.[37] Although this is usually applied to overcome uncertainties in target

position, setup uncertainties, or range uncertainties, it could be used to overcome the limitations of linear accelerator performance. By informing the optimization engine of the possible scenarios that can occur during treatment delivery, the treatment plan can be designed to give an acceptable dose distribution in most or all situations. For this reason,

570   models of treatment delivery accuracy are important.

V. CONCLUSIONS

Estimated uncertainties in dose rate, MLC leaf position and robot target position are shown to have a dosimetric impact of around 1-2% during the arc delivery of SBRT using

575   Cyberknife. The dose rate uncertainty affects the total number of monitor units delivered, which in turn affects the delivered dose. A lag of around 0.5 mm in MLC leaf position affects the delivered dose by approximately 1%, usually with an increase in dose, and an uncertainty in robot pointing has a similar effect. The dose to the PTV is affected most, with a lesser impact on organs at risk that receive less dose in the treatment plan.

580

DISCLOSURE OF CONFLICTS OF INTEREST

595   **REFERENCES**

1. Puataweepong P, Dhanachai M, Hansasuta A, et al. Clinical outcomes of perioptic

    tumors treated with hypofractionated stereotactic radiotherapy using CyberKnife®

    stereotactic radiosurgery. *J Neurooncol.* 2018;139:679-688.

2. Kim N, Lee H, Kim JS, et al. Clinical outcomes of multileaf collimator-based

600   CyberKnife for spine stereotactic body radiation therapy. *Br J Radiol.*

    2017;90:20170523.

3. Que J, Kuo H-T, Lin L-C, et al. Clinical outcomes and prognostic factors of

    cyberknife stereotactic body radiation therapy for unresectable hepatocellular

    carcinoma. *BMC Cancer* 2016;16:451.

605   4. Janvary ZL, Jansen N, Baart V, et al. Clinical outcomes of 130 patients with primary

    and secondary lung tumors treated with Cyberknife robotic stereotactic body

    radiotherapy. *Radiol Oncol.* 2017;51:178-186.

5. Asmerom G, Bourne D, Chappelow J, et al. The design and physical characterization

    of a multileaf collimator for robotic radiosurgery. *Biomed Phys Eng Express*

610   2016;2:017003.

6. Francescon P, Kilby W, Noll JM, Masi L, Satariano N, Russo S. Monte Carlo

    simulated corrections for beam commissioning measurements with circular and MLC

    shaped fields on the CyberKnife M6 System: a study including diode, microchamber,

    point scintillator, and synthetic microdiamond detectors. *Phys Med Biol.*

615   2017;62:1076-1095.

7. Kilby W, Naylor M, Dooley JR, Maurer Jr CR, Sayeh S. A technical overview of the

    CyberKnife system. In: Abedin-Nasab MH, ed. *Handbook of Robotic and Image-*

    Guided Surgery. Amsterdam: Elsevier; 2020:15-38.

8. Bedford JL, Ziegenhein P, Nill S, Oelfke U. Beam selection for stereotactic ablative radiotherapy using Cyberknife with multileaf collimation. *Med Eng Phys.* 2019;64:28-36.

9. Kearney V, Cheung JP, McGuinness C, Solberg TD. CyberArc: a non-coplanar-arc optimization algorithm for CyberKnife. *Phys Med Biol.* 2017;62:5777-5789.

10. Kearney V, Descovich M, Sudhyadhom A, Cheung JP, McGuinness C, Solberg TD. A continuous arc delivery optimization algorithm for CyberKnife m6. *Med Phys.* 2018;45:3861-3870.

11. Yang B, Wong W, Lam W, et al. QA of manipulator-pointing accuracy for CyberKnife using a cylindrical diode array. *Med Phys.* 2018;45:e123.

12. Yang B, Wong WKR, Lam WW, et al. A novel method for monitoring the constancy of beam path accuracy in CyberKnife. *J Appl Clin Med Phys.* 2019;20(5):109-119.

13. Wang L, Lo A, Ho A. Implementation of the electronic portal imaging device for daily CyberKnife quality assurance. *Med Phys.* 2018;45:e327.

14. Wang L, Nelson B. A beam-level delivery accuracy study of the robotic image guided radiosurgery system using a scintillator/CCD phantom. *Med Phys.* 2018;45:e661.

15. Bedford JL, Tsang HS, Nill S, Oelfke U. Treatment planning optimization with beam motion modeling for dynamic arc delivery of SBRT using Cyberknife with multileaf collimation. *Med Phys.* 2019;46:5421-5433.

16. Lukka HR, Pugh SL, Bruner DW, et al. Patient reported outcomes in NRG Oncology RTOG 0938, evaluating two ultrahypofractionated regimens for prostate cancer. *Int J Radiat Oncol Biol Phys.* 2018;102:287-295.

17. Fuller DB, Naitoh J, Lee C, Hardy S, Jin H. Virtual HDR Cyberknife treatment for localized prostatic carcinoma: dosimetry comparison with HDR brachytherapy and preliminary clinical observations. *Int J Radiat Oncol Biol Phys.* 2008;70:1588-1597.

18. Fuller DB, Naitoh J, Mardirossian G. Virtual HDR CyberKnife SBRT for localized prostatic carcinoma: 5-year disease-free survival and toxicity observations. *Front Oncol.* 2014;321:1-7.

19. Bezjak A, Paulus R, Gaspar LE, et al. Safety and efficacy of a five-fraction stereotactic body radiotherapy schedule for centrally located non-small-cell lung cancer: NRG Oncology / RTOG 0813 trial. *J Clin Oncol.* 2019;37.

20. Vautravers-Dewas C, Dewas S, Bonodeau F, et al. Image-guided robotic stereotactic body radiation therapy for liver metastases: is there a dose response relationship? *Int J Radiat Oncol Biol Phys.* 2011;81:e39-e47.

21. Julian TB, Costantino JP, Vicini FA, et al. Early toxicity results with 3-D conformal external beam therapy (CEBT) from the NSABP B-39/RTOG 0413 accelerated partial breast irradiation (APBI) trial. *Int J Radiat Oncol Biol Phys.* 2011;81:S7.

22. Ziegenhein P, Kamerling CP, Bangert M, Kunkel J, Oelfke U. Performance-optimized clinical IMRT planning on modern CPUs. *Phys Med Biol.* 2013;58:3705-3715.

23. Xia P, Verhey LJ. Multileaf collimator leaf sequencing algorithm for intensity modulated beams with multiple static segments. *Med Phys.* 1998;25:1424-1434.

24. Wild E, Bangert M, Nill S, Oelfke U. Noncoplanar VMAT for nasopharyngeal tumors: Plan quality versus treatment time. *Med Phys.* 2015;42:2157-2168.

25. Christiansen E, Heath E, Xu T. Continuous aperture dose calculation and optimization for volumetric modulated arc therapy. *Phys Med Biol.* 2018;63:21NT01.

26. Bedford JL. Treatment planning for volumetric modulated arc therapy. *Med Phys.* 2009;36:5128-5138.

27. Smyth G, Evans PM, Bamber JC, Bedford JL. Recent developments in non-coplanar radiotherapy. *Br J Radiol.* 2019;92:20180908.

28. Smyth G, Evans PM, Bamber JC, et al. Dosimetric accuracy of dynamic couch

670   rotation during volumetric modulated arc therapy (DCR-VMAT) for primary brain

tumours. *Phys Med Biol.* 2019;64:08NT01.

29. Dieterich S, Cavedon C, Chuang CF et al. Report of AAPM TG 135: Quality

assurance for robotic radiosurgery. *Med Phys.* 2011;38:2914-2936.

30. Moore R. CyberKnife. In: Patel I, Weston S, Palmer AL, Mayles WPM, Whittard P,

675   Clements R, Reilly A, Jordan TJ, eds. *Physics Aspects of Quality Control in*

Radiotherapy, IPEM report 81. 2nd ed. York, UK: Institute of Physics and

Engineering in Medicine; 2018:310-339.

31. Otto K. Volumetric modulated arc therapy: IMRT in a single gantry arc. *Med Phys.*

2008;35:310-317.

680 32. Yu CX, Tang G. Intensity-modulated arc therapy: principles, technologies and

clinical implementation. *Phys Med Biol.* 2011;56:R31-R54.

33. Teoh M, Clark CH, Wood K, Whitaker S, Nisbet A. Volumetric modulated arc

therapy: a review of current literature and clinical use in practice. *Br J Radiol.*

2011;84:967-996.

685 34. Ling CC, Zhang P, Archambault Y, Bocanek J, Tang G, LoSasso T. Commissioning

and quality assurance of RapidArc radiotherapy delivery system. *Int J Radiat Oncol*

Biol Phys. 2008;72:575-581.

35. Bedford JL, Warrington AP. Commissioning of volumetric modulated arc therapy

(VMAT). *Int J Radiat Oncol Biol Phys.* 2009;73:537-545.

690 36. Mans A, Schuring D, Arends M, et al. Code of practice for the quality assurance and

control for volumetric modulated arc therapy (Report 24 of the Netherlands

Commission on Radiation Dosimetry). Delft, The Netherlands: Nederlandse

Commissie voor Stralingsdosimetrie; 2015.

37. Unkelbach J, Alber M, Bangert M, et al. Robust radiotherapy planning. *Phys Med*

695   *Biol.* 2018;63:22TR02.